Front. Mech. Eng. 2023, 18(1): 15
https://doi.org/10.1007/s11465-022-0731-1

RESEARCH ARTICLE

Full-field dynamic strain reconstruction of an aero-engine blade from limited displacement responses

Chunyan AO[a,b], Baijie QIAO (✉)[a,b,c], Kai ZHOU[a,b], Lei CHEN[a,b], Shunguo FU[c], Xuefeng CHEN[a,b]

[a] *School of Mechanical Engineering, Xi'an Jiaotong University, Xi'an 710049, China*
[b] *The State Key Laboratory for Manufacturing Systems Engineering, Xi'an 710061, China*
[c] *AECC Sichuan Gas Turbine Establishment, Chengdu 610500, China*

✉ *Corresponding author. E-mail: qiao1224@xjtu.edu.cn (Baijie QIAO)*

ABSTRACT Blade strain distribution and its change with time are crucial for reliability analysis and residual life evaluation in blade vibration tests. Traditional strain measurements are achieved by strain gauges (SGs) in a contact manner at discrete positions on the blades. This study proposes a method of full-field and real-time strain reconstruction of an aero-engine blade based on limited displacement responses. Limited optical measured displacement responses are utilized to reconstruct the full-field strain. The full-field strain distribution is in-time visualized. A displacement-to-strain transformation matrix is derived on the basis of the blade mode shapes in the modal coordinate. The proposed method is validated on an aero-engine blade in numerical and experimental cases. Three discrete vibrational displacement responses measured by laser triangulation sensors are used to reconstruct the full-field strain over the whole operating time. The reconstructed strain responses are compared with the results measured by SGs and numerical simulation. The high consistency between the reconstructed and measured results demonstrates the accurate strain reconstructed by the method. This paper provides a low-cost, real-time, and visualized measurement of blade full-field dynamic strain using displacement response, where the traditional SGs would fail.

KEYWORDS aero-engine blade, displacement response, dynamic strain reconstruction, mode shape, strain gauge

1 Introduction

Dynamic strain due to structural vibration is of great concern in the design, test, and service stages of aero-engine blades. A primary goal in the blade high cycle fatigue (HCF) test is to measure the dynamic strain as an effective parameter for health condition monitoring and residual life evaluation [1–3]. One common strain measurement is achieved by strain gauges (SGs) in a contact manner. Although obtaining the strain response directly, SGs have several drawbacks [4–7]. First, the placement of SG is time consuming, and the measurement quality is uncertain mainly affected by manual operation. Second, SGs are prone to failure because of a continuous measurement with a severe environment or high-level strain. Third, SGs can only measure the strain of discrete and limited points on blades. If more points need to be measured, then more SGs are needed to be stuck intrusively on blades, which may add the mass and damping of small and light-weight structures, thereby changing the dynamic behavior of the blades [8–10]. Therefore, developing a minimal manipulating, long-time reliable, non-contact, and full-field dynamic strain measurement of blades is desirable.

The use of optical techniques enables the non-contact measurement for structural vibration. Digital image correlation (DIC) and scanning laser Doppler vibrometer (SLDV) are two common techniques that can achieve full-field strain measurement [11,12]. The DIC uses high-speed cameras to capture the images of the vibrating object in digital form, which then can be transformed into displacement and strain distribution of the measuring surface of the structure. This technique is mostly used in the measurement of wind turbine blades [13,14]. DIC requires the measuring surface to be sprayed with dense speckles as tracking points. It is time consuming for surface preparation. Besides, the strain spatial resolution using DIC is limited, and small strain may not be identified well. On the contrary, the SLDV is proved to capture small vibration with higher spatial resolution

Received January 17, 2022; accepted August 22, 2022

better, especially the state-of-the-art technique of three-dimension (3D) SLDV [15–17]. Chen et al. [18] applied the 3D SLDV technique on wind turbine blades to determine the complex curvature mode shapes. Vuye et al. [19] used the 3D SLDV to measure the vibratory strain of a full surface of a fan blade, and the scanning results matched well with those from the finite element (FE) model. Maguire and Sever [20] measured the full-field strain distributions of three aero-engine blades by 3D SLDV and compared the results with those from SG measurement. Although 3D SLDV can measure the full-field vibratory strain of aero-engine blades with high resolution, it is also time-consuming because of the dense mesh plan of the measuring surface and the point-by-point scanning process. Vuye et al. [19] recordeded the average measuring time of 1.5 h for the first measurement and 45 min for subsequent measurements when scanning one face of a fan blade. The fundamental reason for such a time consuming way using SLDV is that excessive points must be measured for the full-field strain distribution. The high cost of the 3D SLDV is also another drawback for strain measurement. Recently, Luo et al. [21] measured the deformation of a wind turbine blade using radar technique. Although the proposed technique has lower cost and is faster than SLDV techniques, it can neither complete strain distribution measurement nor achieve real-time measurement. In general, SLDV and radar techniques cannot measure the full-field dynamic strain in real-time or online tests mainly because excessive points need to be measured. If the limited measured responses can be expanded or reconstructed to the full-field response, then the application of the optical technique on the real-time measurement of the blade full-field dynamic strain is promising.

One technique to calculate the full-field response from discrete and limited measurements is the system equivalent reduction expansion process (SEREP) [22]. SEREP provides an expansion technique of displacement and acceleration responses on unmeasured positions, thereby giving perception on the change in the structural dynamic behavior concerning the safety and potential damage [23]. Recently, the dynamic strain, greatly relating to the HCF damage, is also expanded using limited response based on SEREP. Baqersad and Bharadwaj [24] predicted the full-field strain of a 1.52 m-long beam using a handful of strain responses from SG measurement. The predicted strain responses of several points on the beam show a good consistency with the SG results in the time domain. Subsequently, Bharadwaj et al. [25] combined the DIC and SEREP techniques to expand the strain of a long spoiler. The time response assurance criterion (TRAC) was used to evaluate the correlation between the expanded and measured results. Previous studies using expansion techniques on strain-to-strain or displacement-to-displacement reconstruction have shown great success on large-scale wind turbine blades and plates or beams with simple shapes. However, in the above studies, less attention has been paid to the full-field dynamic strain reconstruction of aero-engine blades with complex profiles and shapes using limited displacement responses. The accurate measurement of the displacement caused by the small vibration of blades is the basis for effective strain reconstruction. To date, non-contact measurements by high-precision optical techniques may be optimal. Blade tip timing (BTT) is a system that uses optical fiber sensors to measure the deflection of the rotating blades [26–28]. However, the BTT measurement contains several uncertainties that have not been quantitated [29–31]. These uncertainties may decline the credibility of measured displacement. In this paper, the laser triangulation sensors (optoNCDT 2310-10) from Micro-Epsilon Corporation® are used to measure the blade vibration displacement, which can identify the displacement with a resolution of 0.5 μm and an adjustable measuring frequency up to 49 kHz. This type of laser sensor has been widely used in the industry because of its high precision and relatively low cost [32,33]. In this paper, displacement-to-strain transmissibility is proposed to reconstruct the dynamic strain from limited displacement responses. Three laser triangulation sensors measure the vibration displacement of the blade. The limited displacement responses are used to reconstruct the full-field dynamic strain of the blade in real time. The main contributions of this paper are listed as follows:

1) A full-field strain reconstruction method is proposed to transform the limited displacement responses into strain distribution of an aero-engine blade. The analytical expression of the displacement-to-strain transformation is derived in the modal coordinate.

2) The dynamic strain is reconstructed in the time domain. The full-field strain distribution is visualized by the FE model, which provides credible information for blade structural design improvement and residual life evaluation in blade vibration tests.

3) The blade strain distribution is reconstructed in a low-cost, real-time, and visualized way, where the traditional SGs, DIC, and SLDV techniques would fail.

The paper is outlined as follows. Section 2 discusses reconstruction theory and derives the displacement-to-strain transformation matrix based on the blade mode shapes. Section 3 establishes an accurate FE model of the blade to calculate the mode shapes by modal analysis and presents the experimental preparation and configurations in detail. Section 4 performs two numerical cases based on the FE model to validate the proposed reconstruction technique. After numerical verification, Section 5 executes three sets of experiments on the blade to reconstruct the real-time strain and determine the full-field strain distribution. The reconstructed results are compared with those measured by SGs for validation. Section 6 concludes the work.

2 Reconstruction theory

2.1 Displacement-to-strain transmissibility matrix

The transformation matrix on expanding the measured responses to the unknown locations of the blade can be derived using the SEREP technique. In this paper, a displacement-to-strain transmissibility (DST) matrix is established on the basis of SEREP and blade mode shapes. To establish the motion equation, the blade is considered a proportionally damped system with multiple degrees of freedom. The motion equation can be written as

$$\boldsymbol{M}\ddot{\boldsymbol{x}}(t)+\boldsymbol{C}\dot{\boldsymbol{x}}(t)+\boldsymbol{K}\boldsymbol{x}(t)=\boldsymbol{F}(t), \tag{1}$$

where $\dot{\boldsymbol{x}}(t)$ and $\ddot{\boldsymbol{x}}(t)$ are the first and second derivatives of $\boldsymbol{x}(t)$, $\boldsymbol{M}$, $\boldsymbol{C}$, and $\boldsymbol{K}$ denote the mass matrix, damping matrix, and stiffness matrix, respectively, and t is the response time. Equation (1) can be solved by the FE method. It is assumed that n is the node number of the blade FE model. Generally, for solid elements, each node has three degrees of freedom (the directions of X, Y, and Z). To avoid redundant explanation, n degrees of freedom of the FE model in one direction are considered in Eq. (1). $\boldsymbol{F}_{n\times1}$ is the force vector. $\boldsymbol{x}_{n\times1}(t)$ denotes the displacement response vector. $\boldsymbol{M}$, $\boldsymbol{C}$, and $\boldsymbol{K}$ are all in the size of $(n\times n)$. Notably, $\boldsymbol{C}$ is assumed to be proportional. In this study, Rayleigh damping is adapted and written as

$$\boldsymbol{C}=\alpha\boldsymbol{M}+\beta\boldsymbol{K}, \tag{2}$$

where α is the mass coefficient, and β is the stiffness coefficient, which can be calculated by the measured damping ratio through Eq. (3):

$$\xi_r=\frac{1}{2}\left(\frac{\alpha}{\omega_r}+\beta\omega_r\right), \tag{3}$$

where ξ_r and ω_r are the damping ratio and circular frequency of the rth mode, respectively. By combining the measured data in Table 1 and Eq. (3), Rayleigh damping can be obtained.

Through Eq. (1), the natural frequencies and displacement mode shapes can be obtained by eigenvalue decomposition based on Eq. (4):

$$\left(\boldsymbol{K}-(2\pi f)^2\boldsymbol{M}\right)\boldsymbol{\Phi}=0, \tag{4}$$

where f denotes the natural frequency of the blade, total n natural frequencies $(f_1,f_2,...,f_n)$ can be calculated by solving $\left|\boldsymbol{K}-(2\pi f)^2\boldsymbol{M}\right|=0$. $\boldsymbol{\Phi}=[\boldsymbol{\Phi}_1,\boldsymbol{\Phi}_2,...,\boldsymbol{\Phi}_n]_{n\times n}$ includes n displacement mode shape vectors that correspond to the n natural frequencies. Each element of $\boldsymbol{\Phi}$ is in the size of $(n\times1)$ (e.g, $(\boldsymbol{\Phi}_1)_{n\times1}$). Thus, the n in the column of $\boldsymbol{\Phi}$ denotes the number of mode shapes, whereas n in the row denotes the number of n nodes. Notably, real modal analysis is adopted in this study considering the light damping ratio measured in the test (Table 1). Thus, the calculated mode shape is real, which means that all the nodes of the blade FE model are in phase. When the blade resonates, all the nodes attain maximum/zero deflection simultaneously. To obtain the blade strain mode shapes, the transformation from the displacement mode shape to the strain mode shape is introduced, which can be performed by applying an operator $\boldsymbol{S}$ [34], written as

$$\boldsymbol{S}=\frac{1}{2}\left(\boldsymbol{\nabla}+\boldsymbol{\nabla}^{\mathrm{T}}\right), \tag{5}$$

where $\boldsymbol{\nabla}$ is the linear differential operator [35]. $\boldsymbol{S}$ is applied to the rth displacement mode shape ($(\boldsymbol{\Phi}_r)_{n\times1}$) to calculate the rth strain mode shape ($(\boldsymbol{\Psi}_r)_{n\times1}$), expressed as

$$\boldsymbol{\Psi}_r=\boldsymbol{S}\boldsymbol{\Phi}_r,\quad r=1,2,...,n. \tag{6}$$

Based on the mode superposition method [36], the blade vibration response is contributed by each mode of the blade. The displacement response can be expressed in the frequency domain as

$$\boldsymbol{x}(t)=\sum_{r=1}^{n}\boldsymbol{\Phi}_r\boldsymbol{q}_r^{\mathrm{d}}(t), \tag{7}$$

where $\boldsymbol{q}_r^{\mathrm{d}}(t)$ is the displacement contribution coefficient vector of the rth mode. Similarly, the blade strain response can be superposed by strain mode shapes, written as

$$\boldsymbol{\varepsilon}(t)=\sum_{r=1}^{n}\boldsymbol{\Psi}_r\boldsymbol{q}_r^{\varepsilon}(t), \tag{8}$$

where $\boldsymbol{\varepsilon}_{n\times1}(t)$ is the strain response vector, and $\boldsymbol{q}_r^{\varepsilon}(t)$ is the strain contribution coefficient vector of the rth mode.

Excited by the external force, the blade forced vibration can also be calculated by the frequency response function (FRF) and the external forces [37]. In the frequency domain, the displacement response can be represented as

$$\boldsymbol{x}(\omega)=\boldsymbol{H}(\omega)\boldsymbol{F}(\omega)=\sum_{r=1}^{n}\frac{\boldsymbol{\Phi}_r\boldsymbol{\Phi}_r^{\mathrm{T}}}{K_r-\omega^2M_r+\mathrm{i}\omega C_r}\boldsymbol{F}(\omega), \tag{9}$$

where $\boldsymbol{x}(\omega)$ and $\boldsymbol{F}(\omega)$ are the displacement response and force vectors in the frequency domain, respectively, $\boldsymbol{H}(\omega)$ is the displacement FRF matrix, K_r, M_r, and C_r are the rth modal stiffness, mass, and damping of the blade, i is the imaginary unit, and ω is the exciting frequency. By combining Eqs. (7) and (9), the displacement contribution coefficient vector in the frequency domain $\boldsymbol{q}_r^{\mathrm{d}}(\omega)$ is formulated as

Table 1 First three resonance frequencies obtained by the frequency sweep and FE model and the damping ratios of the first three modes of the blade

Order	Damping ratio/%	Sweeping frequency/Hz	FE model frequency/Hz	Frequency error/%
First	0.02	108.7	109.6	0.8
Second	0.55	468.8	455.5	−2.8
Third	0.02	643.2	641.1	−0.3

$$\boldsymbol{q}_r^{\mathrm{d}}(\omega)=\frac{\boldsymbol{\Phi}_r^{\mathrm{T}}\boldsymbol{F}(\omega)}{K_r-\omega^2M_r+\mathrm{i}\omega C_r}. \tag{10}$$

Based on the operator $\boldsymbol{S}$ in Eq. (6), the strain response of the blade with proportional damping can be derived from the displacement response [38], expressed as

$$\boldsymbol{\varepsilon}(t)=\boldsymbol{S}\boldsymbol{x}(t). \tag{11}$$

By combing Eqs. (6), (8), (9), and (11), the strain response can be rewritten in the frequency domain as

$$\boldsymbol{\varepsilon}(\omega)=\sum_{r=1}^{n}\boldsymbol{\Psi}_r\boldsymbol{q}_r^{\varepsilon}(\omega)=\sum_{r=1}^{n}\frac{\boldsymbol{\Psi}_r\boldsymbol{\Phi}_r^{\mathrm{T}}}{K_r-\omega^2M_r+\mathrm{i}\omega C_r}\boldsymbol{F}(\omega). \tag{12}$$

Through Eq. (12), the strain contribution coefficient vector in the frequency domain $\boldsymbol{q}_r^{\varepsilon}(\omega)$ is formulated as

$$\boldsymbol{q}_r^{\varepsilon}(\omega)=\frac{\boldsymbol{\Phi}_r^{\mathrm{T}}\boldsymbol{F}(\omega)}{K_r-\omega^2M_r+\mathrm{i}\omega C_r}. \tag{13}$$

Equations (10) and (13) show that the strain contribution coefficient vector ($\boldsymbol{q}_r^{\varepsilon}$) is equal to the displacement contribution coefficient vector ($\boldsymbol{q}_r^{\mathrm{d}}$) in the frequency domain. Similarly, in the time domain, the two contribution coefficient vectors are identical to each other based on Fourier transform theory [39]. Thus, in this study, the displacement and strain contribution coefficient vectors of the rth mode are uniformly denoted as $\boldsymbol{q}_r$ ($\boldsymbol{q}_r=\boldsymbol{q}_r^{\mathrm{d}}=\boldsymbol{q}_r^{\varepsilon}$) [24].

Based on the SEREP and mode superposition theories, the full-field displacement and strain response of the blade can be expressed as

$$\boldsymbol{x}_{\mathrm{full}}=\boldsymbol{\Phi}_{\mathrm{full}}\boldsymbol{q}, \tag{14}$$

$$\boldsymbol{\varepsilon}_{\mathrm{full}}=\boldsymbol{\Psi}_{\mathrm{full}}\boldsymbol{q}, \tag{15}$$

where the subscript full denotes the full dimension. $\boldsymbol{x}_{\mathrm{full}}$ and $\boldsymbol{\varepsilon}_{\mathrm{full}}$ are the full-field displacement response and strain response of the blade, respectively. The two full-field responses are in the size of $(n\times p)$. p denotes the number of time steps of the response. $\boldsymbol{\Phi}_{\mathrm{full}}$ and $\boldsymbol{\Psi}_{\mathrm{full}}$ are the displacement mode shapes and strain mode shapes in full dimension, respectively. Considering total m modes contributing to the blade vibration, the size of the full-dimension mode shape matrix is n. $\boldsymbol{q}$ is the mode contribution matrix in the time domain, where $\boldsymbol{q}(t)=[\boldsymbol{q}_1(t),\boldsymbol{q}_2(t),...,\boldsymbol{q}_m(t)]_{m\times p}^{\mathrm{T}}$. In a certain instant, $\boldsymbol{q}$ turns into a mode contribution vector.

In Eq. (14), measuring the displacement response in full dimension is difficult. A set of limited dimensions of response can be easily measured. Thus, the full-field displacement response in Eq. (14) can be divided into the measured response ($\boldsymbol{x}_{\mathrm{mear}}$) and the unmeasured/unknown response ($\boldsymbol{x}_{\mathrm{unkn}}$). The measured dimension is k, and the unmeasured/unknown dimension is j, where $n=k+j$. Correspondingly, the full-field displacement mode shapes can be divided into the mode shape of the measured nodes ($\boldsymbol{\Phi}_{\mathrm{mear}}$) and that of the unmeasured nodes ($\boldsymbol{\Phi}_{\mathrm{unkn}}$). Equation (14) can be rewritten as

$$\boldsymbol{x}_{\mathrm{full}}=\begin{Bmatrix}\boldsymbol{x}_{\mathrm{mear}}\\ \boldsymbol{x}_{\mathrm{unkn}}\end{Bmatrix}=\boldsymbol{\Phi}_{\mathrm{full}}\boldsymbol{q}=\begin{Bmatrix}\boldsymbol{\Phi}_{\mathrm{mear}}\\ \boldsymbol{\Phi}_{\mathrm{unkn}}\end{Bmatrix}\boldsymbol{q}, \tag{16}$$

where the subscript mear and unkn denote the measured dimensions and the unknown dimensions of response, respectively. In Eq. (16), the measured and unknown displacement responses share the same mode contribution vector. Specifically, the measured displacement can be expressed by the mode superposition, written as

$$\boldsymbol{x}_{\mathrm{mear}}=\boldsymbol{\Phi}_{\mathrm{mear}}\boldsymbol{q}. \tag{17}$$

The mode contribution vector $\boldsymbol{q}$ can be calculated using the generalized inverse method, given by

$$\boldsymbol{q}=\boldsymbol{\Phi}_{\mathrm{mear}}^{\dagger}\boldsymbol{x}_{\mathrm{mear}}, \tag{18}$$

where $\boldsymbol{\Phi}_{\mathrm{mear}}^{\dagger}$ is the Moore–Penrose generalized inverse matrix of $\boldsymbol{\Phi}_{\mathrm{mear}}$. When the column rank of $\boldsymbol{\Phi}_{\mathrm{mear}}$ is full, $\boldsymbol{\Phi}_{\mathrm{mear}}^{\dagger}$ can be calculated by [40]

$$\boldsymbol{\Phi}_{\mathrm{mear}}^{\dagger}=(\boldsymbol{\Phi}_{\mathrm{mear}}^{\mathrm{T}}\boldsymbol{\Phi}_{\mathrm{mear}})^{-1}\boldsymbol{\Phi}_{\mathrm{mear}}^{\mathrm{T}}. \tag{19}$$

Based on the least square criterion and Euclidean norm, the calculation model of $\boldsymbol{q}$ is established as

$$\boldsymbol{q}=\arg\min_{q}\|\boldsymbol{x}_{\mathrm{mear}}-\boldsymbol{\Phi}_{\mathrm{mear}}\boldsymbol{q}\|_2^2, \tag{20}$$

where $\|\cdot\|$ is the Euclidean norm. The mode contribution vector $\boldsymbol{q}$ calculated by Eq. (20) is a minimum Euclidean norm solution, which is closest to the real mode contribution vector in theory. The model in Eq. (20) is widely used in the problem of solving the Moore–Penrose generalized inverse matrix [22,24]. The condition for the credible solution of $\boldsymbol{q}$ is that the row number of $\boldsymbol{\Phi}_{\mathrm{mear}}$ is equal or greater than its column number. In the reconstruction, the number of the measured dimensions/nodes k should be equal to or greater than the number of the contributed modes (m). Particularly, when the number of the measured dimensions/nodes k is equal to the number of the contributed mode m, $\boldsymbol{\Phi}_{\mathrm{mear}}^{\dagger}$ is the inverse matrix of $\boldsymbol{\Phi}_{\mathrm{mear}}$, noted as $\boldsymbol{\Phi}_{\mathrm{mear}}^{-1}$. From Eqs. (7)–(16), it is proved that the full-field, measured, and unknown responses of displacement and strain share the identical mode contribution vector $\boldsymbol{q}$.

Through Eq. (20), $\boldsymbol{q}$ can be calculated using the displacement response and mode shape of the measured points. By combining Eqs. (14), (15), and (20), the full-field displacement and strain responses can be reconstructed by Eqs. (21) and (22), which are expressed as

$$\boldsymbol{x}_{\mathrm{full}}=\boldsymbol{\Phi}_{\mathrm{full}}\boldsymbol{\Phi}_{\mathrm{mear}}^{\dagger}\boldsymbol{x}_{\mathrm{mear}}, \tag{21}$$

$$\boldsymbol{\varepsilon}_{\mathrm{full}}=\boldsymbol{\Psi}_{\mathrm{full}}\boldsymbol{\Phi}_{\mathrm{mear}}^{\dagger}\boldsymbol{x}_{\mathrm{mear}}. \tag{22}$$

This study focuses on the full-field strain reconstruction considering the importance of dynamic strain for reliability analysis and residual life evaluation in blade vibration tests. Based on Eq. (22), the DST matrix is ultimately derived as

$$\boldsymbol{T} = \boldsymbol{\Psi}_{\text{full}} \boldsymbol{\Phi}^{\dagger}_{\text{mear}}, \tag{23}$$

where $\boldsymbol{T}$ denotes the displacement-to-strain transmissibility matrix, which can reconstruct the full-field strain of the blade using a limited measured displacement response. For the measurements in Cartesian coordinate system, the blade displacement $\boldsymbol{x}$ includes three components in the directions of X, Y, and Z ($\boldsymbol{x}_x$, $\boldsymbol{x}_y$, and $\boldsymbol{x}_z$). The blade strain $\boldsymbol{\varepsilon}$ contains three normal strains defined as $\boldsymbol{\varepsilon}_x$, $\boldsymbol{\varepsilon}_y$, and $\boldsymbol{\varepsilon}_z$ and three shear strains defined as $\boldsymbol{\gamma}_{xy}$, $\boldsymbol{\gamma}_{yz}$, and $\boldsymbol{\gamma}_{xz}$. Correspondingly, the blade displacement mode shape $\boldsymbol{\Phi}$ and strain mode shape $\boldsymbol{\Psi}$ also have three displacement components ($\boldsymbol{\Phi}_x$, $\boldsymbol{\Phi}_y$, and $\boldsymbol{\Phi}_z$) and six strain components ($\boldsymbol{\Psi}_x$, $\boldsymbol{\Psi}_y$, $\boldsymbol{\Psi}_z$, $\boldsymbol{\Psi}_{xy}$, $\boldsymbol{\Psi}_{yz}$, and $\boldsymbol{\Psi}_{xz}$). The proposed method has the advantage to reconstruct the normal and shear strains of the vibrational blade.

The condition for the solution of Eq. (23) is that the measured dimension (the row number of $\boldsymbol{\Phi}_{\text{mear}}$) should be equal or greater than the considered modes (the column number of $\boldsymbol{\Phi}_{\text{mear}}$). According to mode superposition theory, not all n mode shapes need to be superposed to compute the response. The consideration of the desired modes, which mainly contribute to the response, will lead to enough accurate results with low computation complexity. For aero-engine fan blades, the lower modes are easier to be excited than the higher modes because of the usual low-frequency bandwidth of the excitations generated by flutter, stall, and surge [41,42]. In this paper, the first three modes of the blade, which is valid for practical operation in engineering, are considered [43]. The full-field strain reconstruction can be executed in the time and frequency domains.

2.2 Reconstruction process

The proposed reconstruction technique is outlined in Fig. 1. In Step 1, the FE model of the blade is established. The displacement and strain mode shapes are computed through modal analysis on the FE model. The DST concerning the measured points and full-field model is derived on the basis of the mode shapes. In Step 2, the real-time displacement responses are measured by three laser triangulation sensors. Simultaneously, SGs are used to measure the strain responses for later comparison with the reconstructed results. In Step 3, combining the DST and the limited displacement responses, the full-field strain of the blade is reconstructed in the time domain. In

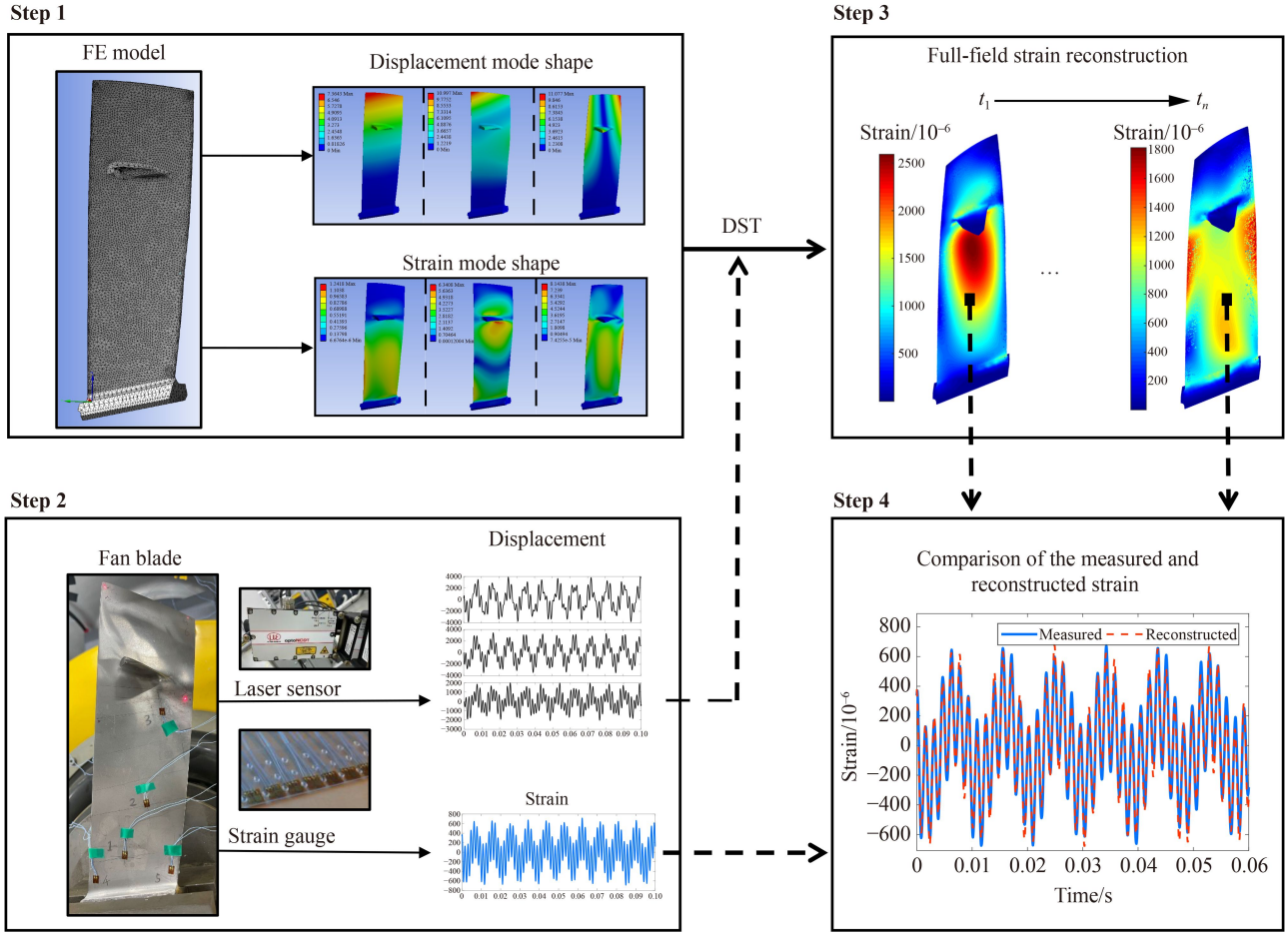

Fig. 1 Process of full-field dynamic strain reconstruction on an aero-engine blade using limited displacement.

Step 4, for validation, the reconstructed strain responses are compared with the SG measured results.

Two additional pieces of work are worth mentioning. The first one is to guarantee a good consistency between the FE model and the physical testing blade. The FE model is validated and updated according to the experimental results by a frequency sweep of the blade on a shaking table. The other is that the measuring direction of the SG changes at different locations on the blade because of the twisting profile and surface of the blade. The reconstructed strain responses on the global coordinate of the blade are needed to be transformed to the local coordinate of the stuck SG for an effective comparison [44]. Illustrating with the stress transform, Fig. 2 shows the stress in a global coordinate system (x, y, z) and the stress in a local coordinate system (x',y',z') after a rotation. The angle between one axis in the local coordinate and the other in the global coordinate is defined as θ (e.g., $\theta_{x'x}$ is the angle between the local x'-axis and the global x-axis). The stress $\boldsymbol{\sigma}$ in a matrix form in a global coordinate system is

$$\boldsymbol{\sigma} = \begin{bmatrix} \sigma_x & \tau_{xy} & \tau_{xz} \\ \tau_{xy} & \sigma_y & \tau_{yz} \\ \tau_{xz} & \tau_{yz} & \sigma_z \end{bmatrix}, \tag{24}$$

where $\boldsymbol{\sigma}$ is the stress matrix, σ_x, σ_y, and σ_z denote the normal stresses in the x, y, and z directions, respectively, and τ_{xy}, τ_{yz}, and τ_{xz} denote the shear stresses in the xy, yz, and xz directions, respectively. The transformation between stress $\boldsymbol{\sigma}'$ in SG local coordinate system and $\boldsymbol{\sigma}$ in the global coordinate system is formulated as

$$\boldsymbol{\sigma}' = \boldsymbol{P}\boldsymbol{\sigma}\boldsymbol{P}^{\mathrm{T}}, \tag{25}$$

where $\boldsymbol{\sigma}' = \begin{bmatrix} \sigma_{x'} & \tau_{x'y'} & \tau_{x'z'} \\ \tau_{x'y'} & \sigma_{y'} & \tau_{y'z'} \\ \tau_{x'z'} & \tau_{y'z'} & \sigma_{z'} \end{bmatrix}$, and the transform matrix $\boldsymbol{P} = \begin{bmatrix} \cos\theta_{x'x} & \cos\theta_{x'y} & \cos\theta_{x'z} \\ \cos\theta_{y'x} & \cos\theta_{y'y} & \cos\theta_{y'z} \\ \cos\theta_{z'x} & \cos\theta_{z'y} & \cos\theta_{z'z} \end{bmatrix}$. $\sigma_{x'}$, $\sigma_{y'}$, and $\sigma_{z'}$ are three normal stresses in the local coordinate. $\tau_{x'y'}$, $\tau_{y'z'}$, and $\tau_{x'z'}$ are three shear stresses in the local coordinate. Similarly, the strain $\boldsymbol{\varepsilon}'$ in SG local coordinate system and $\boldsymbol{\varepsilon}$ in the global coordinate system have the same relationship, written as

$$\boldsymbol{\varepsilon}' = \boldsymbol{P}\boldsymbol{\varepsilon}\boldsymbol{P}^{\mathrm{T}}, \tag{26}$$

where $\boldsymbol{\varepsilon} = \begin{bmatrix} \varepsilon_x & \frac{\gamma_{xy}}{2} & \frac{\gamma_{xz}}{2} \\ \frac{\gamma_{xy}}{2} & \varepsilon_y & \frac{\gamma_{yz}}{2} \\ \frac{\gamma_{xz}}{2} & \frac{\gamma_{yz}}{2} & \varepsilon_z \end{bmatrix}$, and $\boldsymbol{\varepsilon}' = \begin{bmatrix} \varepsilon_{x'} & \frac{\gamma_{x'y'}}{2} & \frac{\gamma_{x'z'}}{2} \\ \frac{\gamma_{x'y'}}{2} & \varepsilon_{y'} & \frac{\gamma_{y'z'}}{2} \\ \frac{\gamma_{x'z'}}{2} & \frac{\gamma_{y'z'}}{2} & \varepsilon_{z'} \end{bmatrix}$.

In the global coordinate, ε_x, ε_y, and ε_z denote the normal strains of the x, y, and z directions, respectively. γ_{xy}, γ_{yz}, and γ_{xz} denote the shear strains of the xy, yz, and xz directions, respectively. Similarly, $\varepsilon_{x'}$, $\varepsilon_{y'}$, $\varepsilon_{z'}$, $\gamma_{x'y'}$, $\gamma_{y'z'}$, and $\gamma_{x'z'}$ are the normal and shear strains in the local coordinate. The equivalent strain based on von Mises yield criterion calculated by the FE method can clearly reflect the blade dynamic behavior and help engineers to find the most dangerous field on the model [45,46]. The equivalent strain ε_e can be calculated by

$$\varepsilon_e = \sqrt{\frac{2}{9}\left[(\varepsilon_x-\varepsilon_y)^2+(\varepsilon_y-\varepsilon_z)^2+(\varepsilon_x-\varepsilon_z)^2+6\left(\gamma_{xy}^2+\gamma_{xz}^2+\gamma_{yz}^2\right)\right]}. \tag{27}$$

3 Experimental object and FE analysis

3.1 Experimental object and setup

To validate the proposed reconstruction technique, an

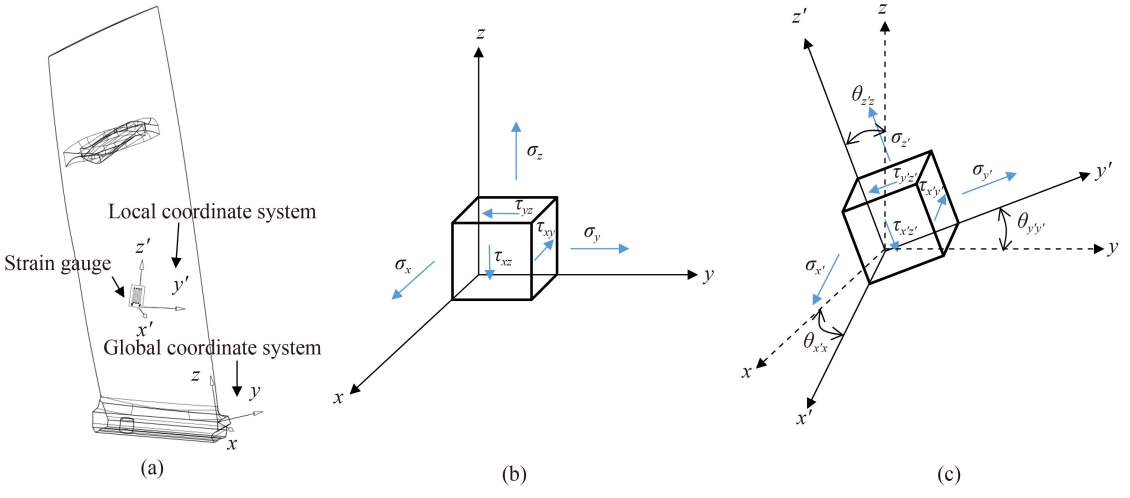

Fig. 2 Stress in global and local coordinate systems of the blade: (a) blade attached with a strain gauge, (b) stress in the global coordinate system, and (c) stress in the local coordinate system after a rotation.

experimental rig involving a fan blade, an exciting system, and a measuring system is set up in this study. Figure 3 shows the main experimental configurations. Instead of the full-field measurement for a whole surface, three discrete points on the blade are arranged for the real-time displacement response measurement by three laser triangulation sensors (optoNCDT 2310-10) from Micro-Epsilon Corporation®. The displacement measuring points are marked as D1, D2, and D3. The three displacement responses are utilized to reconstruct the full-field dynamic strain of the blade. Three SGs from Hanzhong Jingce Electric Appliance Corporation® are attached on the concave surface to measure the real-time strain response. The strain measuring points are marked as SG1, SG2, and SG3. The displacement and strain sensors are connected to a data acquisition system with eight channels from DEWESoft Corporation®.

In the experiments, the blade root is fixed by a specially designed fixture. The blade fixture is clamped on a shaking table by bolts. Based on the credible fixation of the blade on the shaking table through the fixture, the excitations are loaded on the blade through the shaking table controlled by a supporting controller and software. The shaking table, controller, and software are from ECON Technology Corporation®. In addition, an acceleration sensor from Dytran Instruments Corporation® is used to measure the acceleration of the shaking table and provide feedback for closed-loop control of the test.

3.2 Model validation and modal analysis

The reconstruction technique is based on the blade mode shapes by modal analysis on the FE model. A highly consistent FE model relating to the testing blade would lead to an accurate reconstruction result. In this study, the FE model is validated and updated through the results of a frequency sweep of the blade on the shaking table. First, a coarse sweep from 0–1000 Hz with a speed of 1 Hz/s is executed to determine the resonance region. The frequencies of approximately 109, 468, and 643 Hz are found to be the first three resonance frequencies of the blade. Then, three fine sweeps at the frequency bands of 100–120, 455–475, and 630–660 Hz with a speed of 0.25 Hz/s are performed to determine the accurate resonance frequencies of the blade. The transfer function curves by the frequency sweep are shown in Fig. 4.

Based on the designed 3D model of the blade, the FE model is established in ANSYS APDL by tetrahedral meshing with the solid element. Solid 185 and Solid 186 are two types of solid elements [47]. Compared with Solid 185, Solid 186 is a higher order element that includes more nodes, which would lead to a more accurate result from the FE model than Solid 185 when the blade model is meshed by an identical number of elements. In this study, based on the Solid 186 with the element size of 1 mm, the blade FE model is established by a dense meshing with a total of 51200 elements and 94780 nodes (the upper left plot of Fig. 1), which is valid for an accurate FE model of an aero-engine fan blade [48]. The blade is made of Ti–6.5Al–3.5Mo–1.5Zr–0.3Si with a mass density of 4510 kg/m^3, Young's modulus of 123 GPa, and Poisson's ratio of 0.33. The boundary condition has great effects on the FE model analysis results. In the experiments, the blade root is fixed with

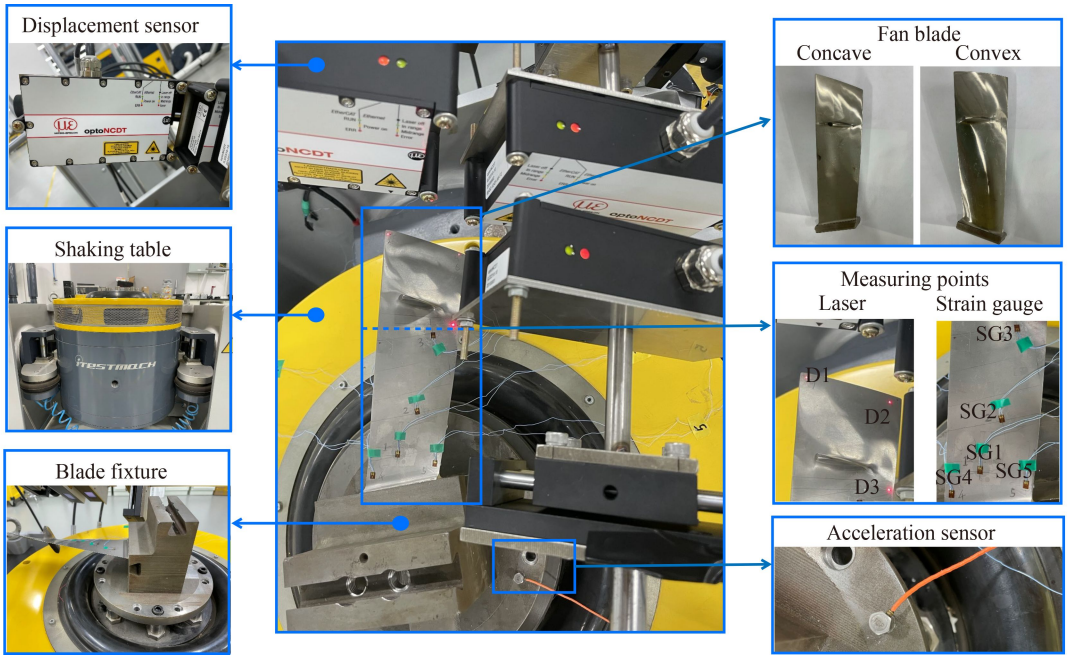

Fig. 3 Experimental configurations for validating the full-field dynamic strain reconstruction technique.

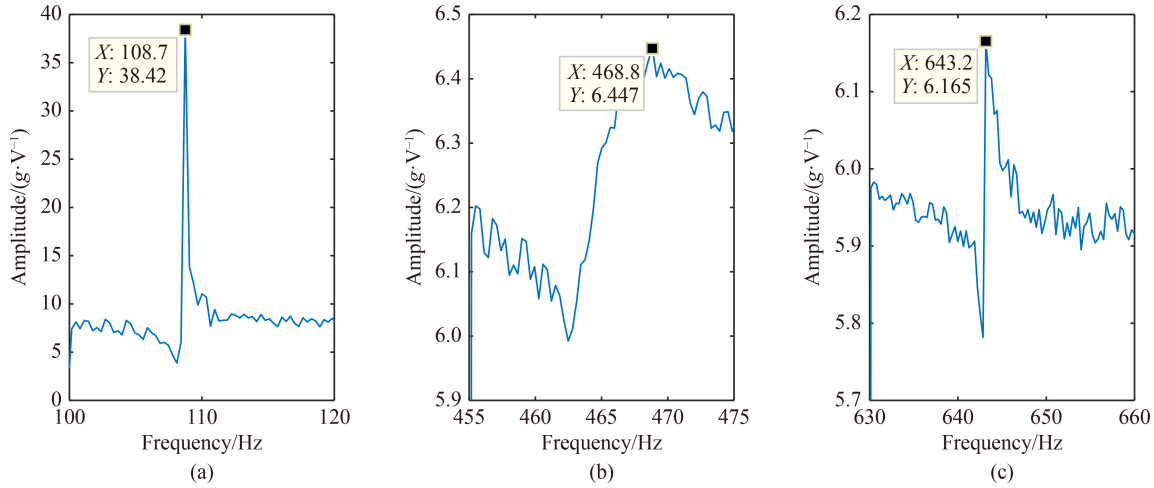

Fig. 4 First three resonance frequencies by the frequency sweep: (a) first, (b) second, and (c) third.

bolts on the fixture, but the definite preload and rigid constraint on the root face are unknown. The boundary condition of the FE model can affect the analysis results. The boundary condition that is close to the experimental condition can lead to an accurate result. Thus, adjusting the boundary condition on the FE model for validation and updating is effective. Four side faces on the root of the FE model are applied with fixed supports. The resonance frequencies of the blade by the frequency sweep test are referred to in this work. Table 1 lists the first three natural frequencies of the updated FE model compared with the results from the frequency sweep. In theory, the damped frequency measured in the test is smaller than that from the FE model. However, an inevitable manufacturing error exists between the physical blade and FE model [16]. The frequency errors of the first three modes between the test and the updated FE model are 0.8%, –2.8%, and –0.3%, respectively, which is acceptable and shows good consistency between the FE model and the testing blade [19]. Based on the FE model, the first three displacement and strain mode shapes of the blade are obtained through modal analysis. Figure 5 portrays the scaled mode shapes of the vector-sum displacement and equivalent strain.

4 Numerical validation

Two numerical cases are performed to validate the merits of the proposed full-field strain reconstruction method on aero-engine blades. One is the reconstruction when the blade vibrates under a single mode excited by a single sinusoidal force. The other is the reconstruction when the blade vibrates under multiple modes excited by a complex sinusoidal force. The mass matrix $\boldsymbol{M}$ and stiffness matrix $\boldsymbol{K}$ of the blade are extracted from the FE model. Based on Eqs. (2) and (3) and Table 1, the mass coefficient (α) and stiffness coefficient (β) are calculated using the damping ratios and natural frequencies of the first and third modes, where $\alpha = 23.24$ and $\beta = 8.48 \times 10^{-6}$. The full-field responses are calculated by solving Eq. (1) using the Newmark-β method. The mode shapes are also calculated by modal analysis, and the DST matrix is derived. The discrete displacement responses of the limited points (e.g., D1, D2, and D3 in Fig. 3) are extracted to reconstruct the full-field strain. The reconstructed strain responses of three SG points (e.g., SG1, SG2, and SG3 in Fig. 3) are compared with the measured ones, which are those calculated by Eq. (1). TRAC is a parameter used to evaluate the correlation between two time-traced responses [25]. The TRAC is defined as

$$\mathrm{TRAC} = \frac{(\boldsymbol{\varepsilon}_{\mathrm{mear}}\boldsymbol{\varepsilon}_{\mathrm{recs}}^{\mathrm{T}})^2}{(\boldsymbol{\varepsilon}_{\mathrm{mear}}\boldsymbol{\varepsilon}_{\mathrm{mear}}^{\mathrm{T}})(\boldsymbol{\varepsilon}_{\mathrm{recs}}\boldsymbol{\varepsilon}_{\mathrm{recs}}^{\mathrm{T}})}, \tag{28}$$

where $\boldsymbol{\varepsilon}_{\mathrm{mear}}$ and $\boldsymbol{\varepsilon}_{\mathrm{recs}}$ denote the measured/simulated and reconstructed strain responses in the time domain, respectively. TRAC values close to 1.0 indicate a strong similarity, whereas the values close to 0.0 indicate minimal or no similarity. Besides the evaluation of the time-traced response, TRAC can also be used to evaluate the correlation of the full-field strain distributions from reconstruction and simulation at each time instance. Then, $\boldsymbol{\varepsilon}_{\mathrm{mear}}$ and $\boldsymbol{\varepsilon}_{\mathrm{recs}}$ in Eq. (28) can be replaced by the full-field strain matrixes at a certain time by simulation and reconstruction, respectively. In this paper, TRAC is used to evaluate the reconstructed and measured/simulated strain responses, including the time-traced and full-field results.

4.1 Single sinusoidal excitation

In this case, the force F is loaded at the blade tip to excite the first mode resonance of the blade. F is formulated as

$$F = \sin(2\pi f_1 t), \tag{29}$$

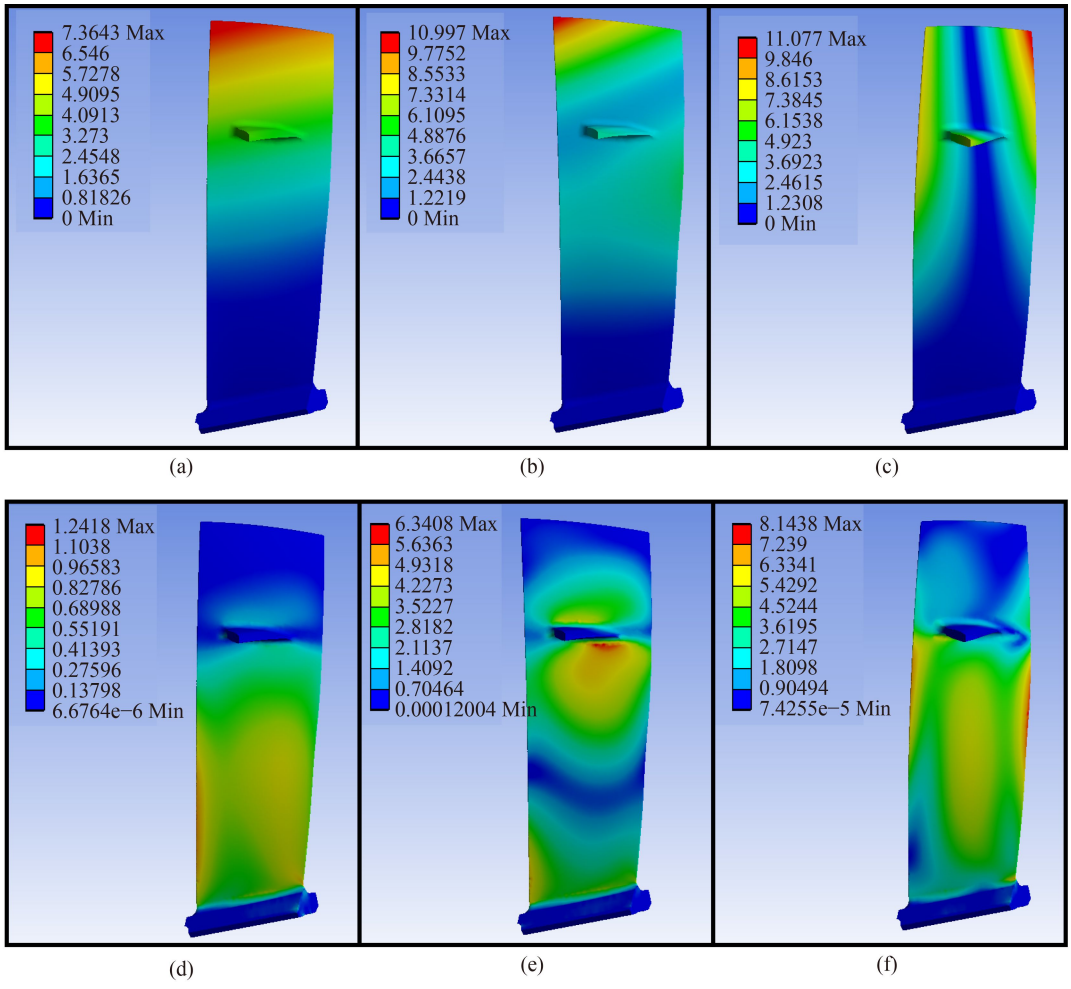

Fig. 5 First three vector-sum displacement and equivalent strain mode shapes of the blade finite element model: (a) the first, (b) the second, and (c) the third displacement mode shape; (d) the first, (e) the second, and (f) the third strain mode shape.

where f_1 is the first natural frequency of the blade. The amplitude of the sinusoidal excitation is 1 N. The blade responses that lasts for 1 s are calculated at a sampling frequency of 16384 Hz. The first displacement and strain mode shapes of the blade are considered in the DST because the first mode resonance is excited. Combining the three displacement responses and the DST, the full-field dynamic strain is reconstructed, and the strain distribution is obtained. Figure 6 shows the full-field results of equivalent strain at 0.5 s and three local comparisons between the reconstructed and measured strain responses of SG points over a period of approximately 0.5 s. The measured strain responses in numerical cases simulate the SG measurement in the local coordinate system. The SG strain values in the time-traced plot may not be equal to those shown in the contour plot of the equivalent strain. Each contour plot of the strain distribution is attached with a color bar to show the different strain levels with various colors. The color on the top of the bar denotes the maximum strain, whereas the color on the bottom of the bar denotes the minimum strain. In general, the reconstructed full-field strain distribution shows a good match with the calculated one by simulation. The time-traced curves of the measured and reconstructed strain responses of three SG points also show high consistency, with all the TRACs equal to 1, thereby validating the proposed method when the blade vibrates under a single mode. Besides, the TRACs of the full-field strain between the reconstruction and simulation at 0.2, 0.4, 0.5, 0.6, and 0.8 s are listed in Table 2. The high correlation between the reconstructed and simulated strain distributions also indicates the effectiveness of the proposed method.

4.2 Complex sinusoidal excitation

The blade multi-mode vibration can be excited by a complex sinusoidal force where the multiple vibratory frequencies of the force are equal to the natural frequencies of the blade. In this paper, the vibration that consists of the first three modes of the blade is aimed to be excited. The force F is expressed as

$$F = \sin(2\pi f_1 t) + 5\sin(2\pi f_2 t) + 15\sin(2\pi f_3 t), \qquad (30)$$

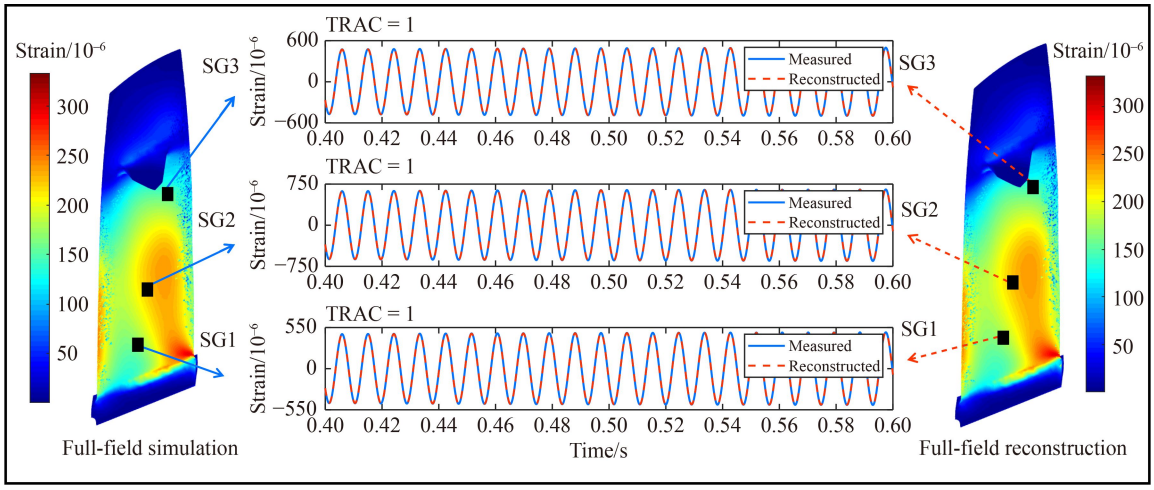

Fig. 6 Comparison of the calculated and reconstructed strains, including the full-field comparison and local comparisons of three SG points when the single-mode vibration occurs, via simulation. SG: strain gauge, TRAC: time response assurance criterion.

Table 2 TRACs of the reconstructed and simulated full-field strain at different instants

Time/s	Single TRAC	Complex TRAC
0.2	1.00	0.99
0.4	1.00	0.99
0.5	1.00	0.99
0.6	1.00	1.00
0.8	1.00	0.99

where f_2 and f_3 are the second and third natural frequencies of the blade, respectively. Notably, the high-order modes are usually more difficult to excite than the first mode. Thus, the amplitudes of the force components at f_2 and f_3 are set as 5 and 15 N, respectively. In this case, the first three mode shapes are considered in the DST for an accurate reconstruction. Figure 7 shows the full-field results of equivalent strain at 0.5 s and three local comparisons between the reconstructed and measured strains of SG points over a period of time around 0.5 s. The TRAC values of the three SG points are equal to 1, which indicates the high consistency between the measured and reconstructed strain responses. At 0.2, 0.4, 0.5, 0.6, and 0.8 s, the TRACs of the full-field strain are calculated by reconstruction and simulation and listed in Table 2. All the TRACs are close to or equal to 1, thereby demonstrating the effectiveness of the proposed methods under blade multi-mode vibration. In general, the complex sinusoidal excitation case demonstrates the applicability of the proposed method when the blade vibrates under multiple modes.

The snapshots of the blade strain distribution at 0.2, 0.4, 0.6, and 0.8 s of single-mode vibration are shown in Fig. 8(a). The four snapshots are identical but have different strain levels (the left color bar), suggesting that the position with max strain is unchanged. However, when the blade is under multi-mode vibration, the snapshots of the strain distribution at four instants are different (Fig. 8(b)), which means that the strain distribution and the position with the max strain of the blade are changing in the time domain. In this case, traditional SGs may fail to monitor the max strain during the blade operation effectively. In contrast to the SG measurement, the proposed method can reconstruct the full-field strain of the blades under single-mode and multi-mode vibrations.

5 Experimental validation

To verify the accuracy of the reconstructed strain using the proposed method, three experimental cases are performed on the basis of the experimental rig shown in Fig. 3 (in Subsection 3.1). The first case excites the single-mode vibration of the blade. The second one excites the multi-mode vibration of the blade, including the first three modes. The third one applies impact forces on the blade to test the reconstruction method when the blade response is broadband and damped. The exciting forces with different oscillatory frequencies and amplitudes are generated by the controller and corresponding software. The amplitude of the force is determined by the acceleration outputted to the shaking table. On the shaking table, the blade generates forced vibration at the set frequency and acceleration. During the vibration, the real-time displacement and strain responses for 15 s are sampled by the laser sensors and SGs with a sampling frequency of 20 kHz, respectively. Based on the proposed method, the full-field dynamic strain of the blade is reconstructed using the non-contact displacement data. The reconstructed strain responses are compared with those measured by SGs. TRAC is used to evaluate the consistency between the reconstructed and measured results.

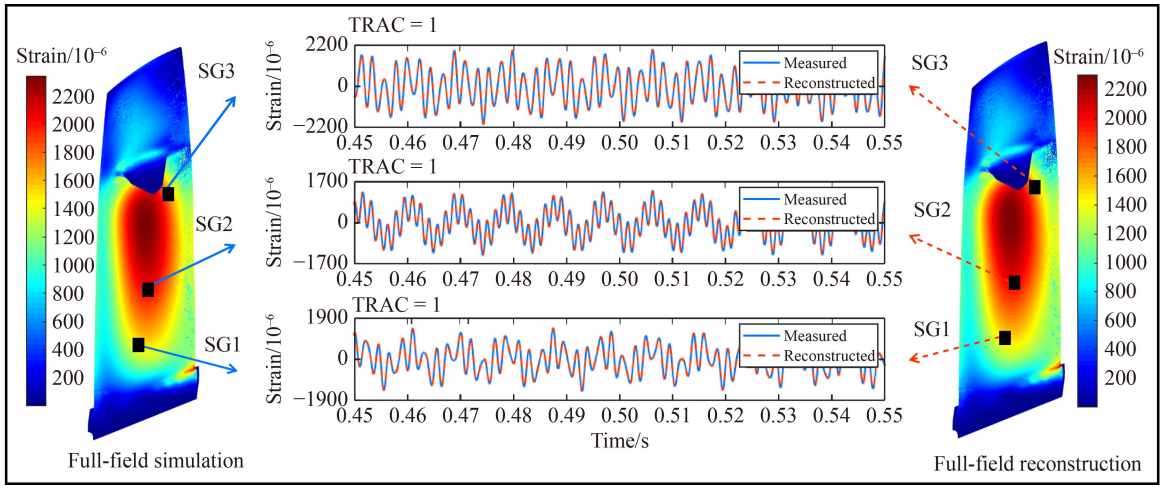

Fig. 7 Comparison of the calculated strain by simulation and the reconstructed strain, including the full-field comparison and local comparison of three SG points when the multi-mode vibration occurs. SG: strain gauge, TRAC: time response assurance criterion.

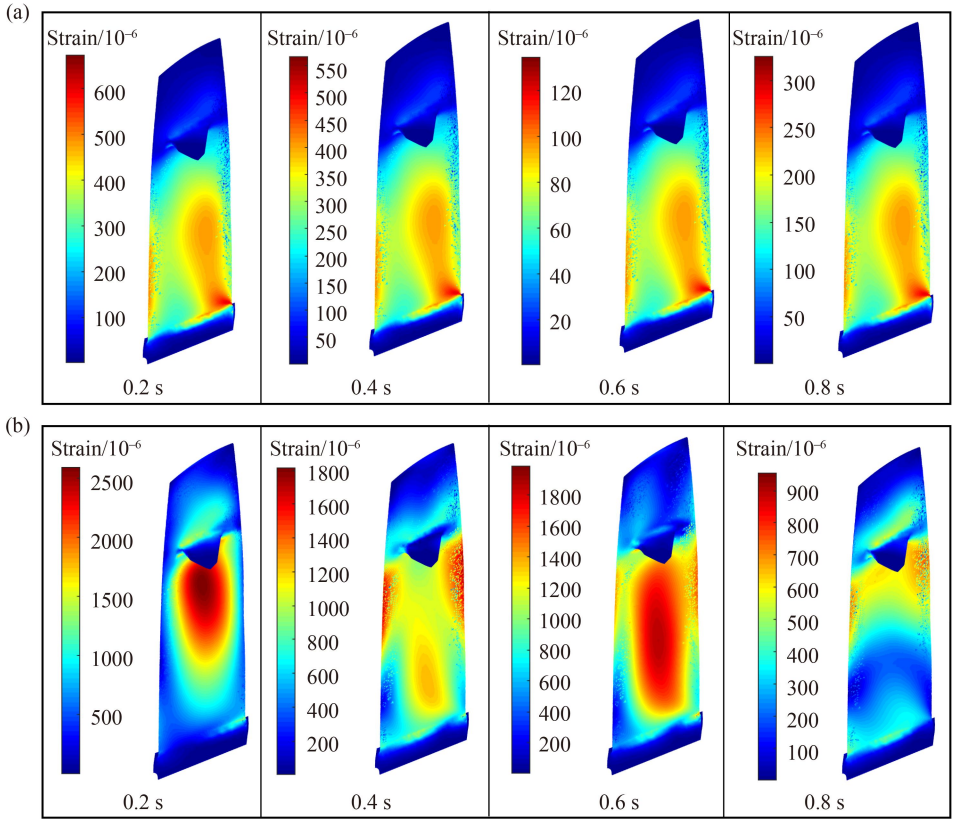

Fig. 8 Strain distributions of the blade in the (a) single-mode vibration and (b) multi-mode vibration at 0.2, 0.4, 0.6, and 0.8 s, respectively.

5.1 Single sinusoidal excitation

In this test, a sinusoidal force at a frequency of 108.7 Hz is outputted to the shaking table with an acceleration of $0.2g$ (g = 9.8 m/s^2). The forced vibration of the blade is the first-mode resonance. The non-contact displacement responses are used to reconstruct the full-field dynamic strain. Figure 9 shows the reconstructed full-field results of the equivalent strain at 7 s and five local comparisons between the reconstructed and SG-measured strain over a period of time around 7 s. The TRACs of the five points are 0.999, 0.998, 0.999, 0.997, and 0.996, respectively. In theory, all the TRACs are supposed to be 1. The small error in TRAC may be caused by the light damping of the blade, which can lead to minimal deviation in phase for the vibration of each point on blades. In general, the

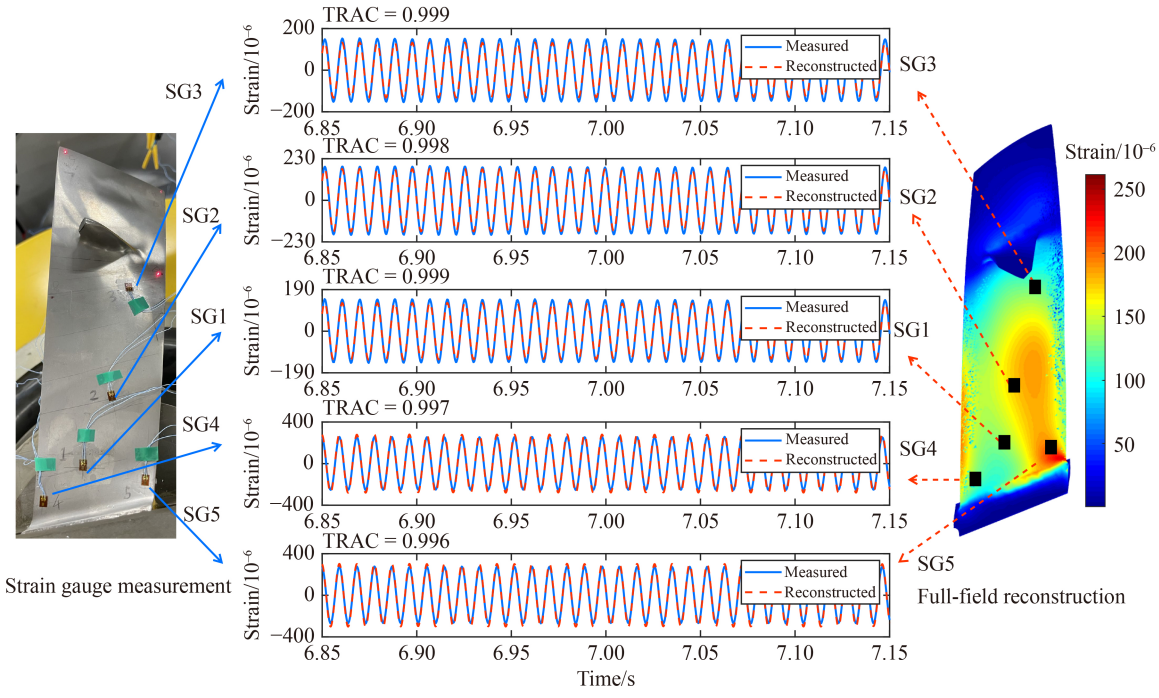

Fig. 9 Comparison of the measured strain by SGs and the reconstructed full-field strain when the blade vibrates under a single mode. SG: strain gauge, TRAC: time response assurance criterion.

TRACs of the five points are almost close to 1, which demonstrates the high consistency between the reconstructed and measured results. Although the full-field strain cannot be measured in the current paper, the reconstructed strain distribution of the blade is very similar to the distribution in the numerical case of single sinusoidal excitation in Subsection 4.1 (Fig. 8), which also indicates the accurate strain using the reconstruction method.

5.2 Complex sinusoidal excitation

To excite the multi-mode vibration of the blade, a complex force that consists of three components at the first three natural frequencies of the blade is generated to control the shaking table. In this case, the blade on the shaking table is prone to vibrate under multiple modes. The first mode in the vibration can be easily excited with small acceleration or input energy. However, the excitation of the higher-order mode of the blade needs higher acceleration. In this test, the accelerations of the three components at the frequencies of 108.7, 468.8, and 643.2 Hz are set as 0.2*g*, 12*g*, and 10*g*, respectively. Based on the proposed method, three displacement responses measured by laser sensors are transformed into the full-field strain of the blade. The first three mode shapes of the blade are considered in the transformation matrix DST for an accurate reconstruction. A low-pass filter at a cutoff frequency of 1000 Hz is imposed on the measured data to filter noise.

Figure 10 shows the reconstructed full-field results of equivalent strain at 7 s and five local comparisons between the reconstructed and SG-measured strains over a period of approximately 7 s. In general, the reconstructed strain responses of five points match well with the SG measurements in the time domain. All the TRACs are close to 1, which demonstrates the accurate strain reconstructed by the proposed method when the blade vibrates under multiple modes. To validate the change in blade strain distribution under multi-mode vibration, four contour plots of the strain distribution at 6.2, 6.8, 7.4, and 8 s are shown in Fig. 11. The distribution and the position with the max strain on blade are changed with time. The change in the strain response seems to be periodical, which can be seen from the time-traced results in Fig. 10. Although such a change may be cycled within a period of time, it would lead to incomplete strain data using discrete measurements by SGs in engineering practice. The method proposed in this paper provides an access to acquire the strain distribution at any operation time using limited displacement responses. The similarities between the experimental distributions at 6.8 and 8 s in Fig. 11 and the numerical distribution at 0.4 and 0.6 s in Fig. 8(b) also demonstrate the accuracy of the reconstructed strain of the blade in multi-mode vibration.

5.3 Impact excitation

To verify the proposed reconstruction method when the blade response is broadband and damped, an impact force test is performed on the blade. Several impact forces are

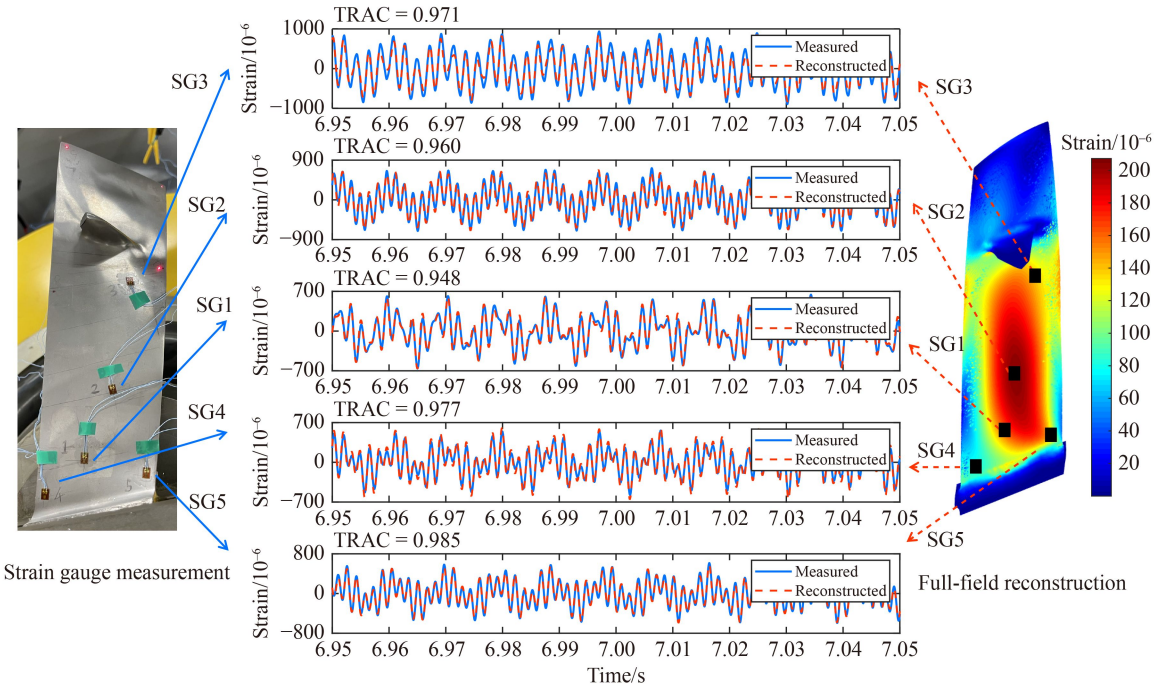

Fig. 10 Comparison of the measured strain by SGs and the reconstructed full-field strain when the blade vibrates under multiple modes. SG: strain gauge, TRAC: time response assurance criterion.

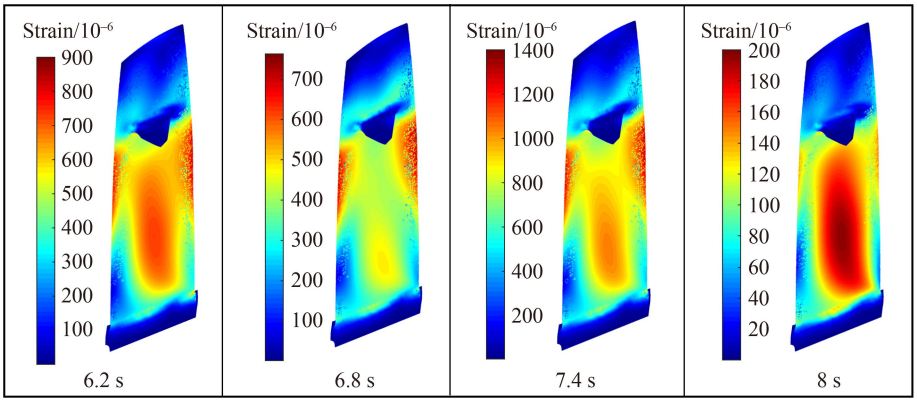

Fig. 11 Different reconstructed strain distributions of the blade in the multi-mode vibration at 6.2, 6.8, 7.4, and 8 s, respectively.

successively loaded on the blade. The response is damped over a period of time after each impact. The displacement and strain responses are sampled for 15 s simultaneously. Figure 12 shows the reconstructed results of five SG points compared with the measured ones when the blade is excited by one impact during 0–5.2 s. Five TRACs are greater than 0.94, which demonstrates the consistency of the reconstructed and measured strain in the time domain. The plot in the right of Fig. 12 gives an expanded view of the time-traced comparison around 2 s. A slight deviation is observed in the amplitude of point SG3 (plot in the top right), which may be caused by the uncertainty from SG. As the previous presentation in this paper, the manual operation on sticking SG greatly affects the measuring quality and position of the SG on blades. In this study, the angular deflection of the SG on the twisting surface is considered by establishing the local coordinate for SG. The correction of the measuring angle decreases the uncertainty in some degree. Generally, the deviation in amplitude is acceptable. The high consistency between the reconstructed and measured results implies the accuracy of the proposed method on strain prediction.

6 Conclusions

A method is proposed in this paper to reconstruct the full-field dynamic strain of aero-engine blades using limited displacement responses. The proposed reconstruction method can not only predict the strain distribution of the

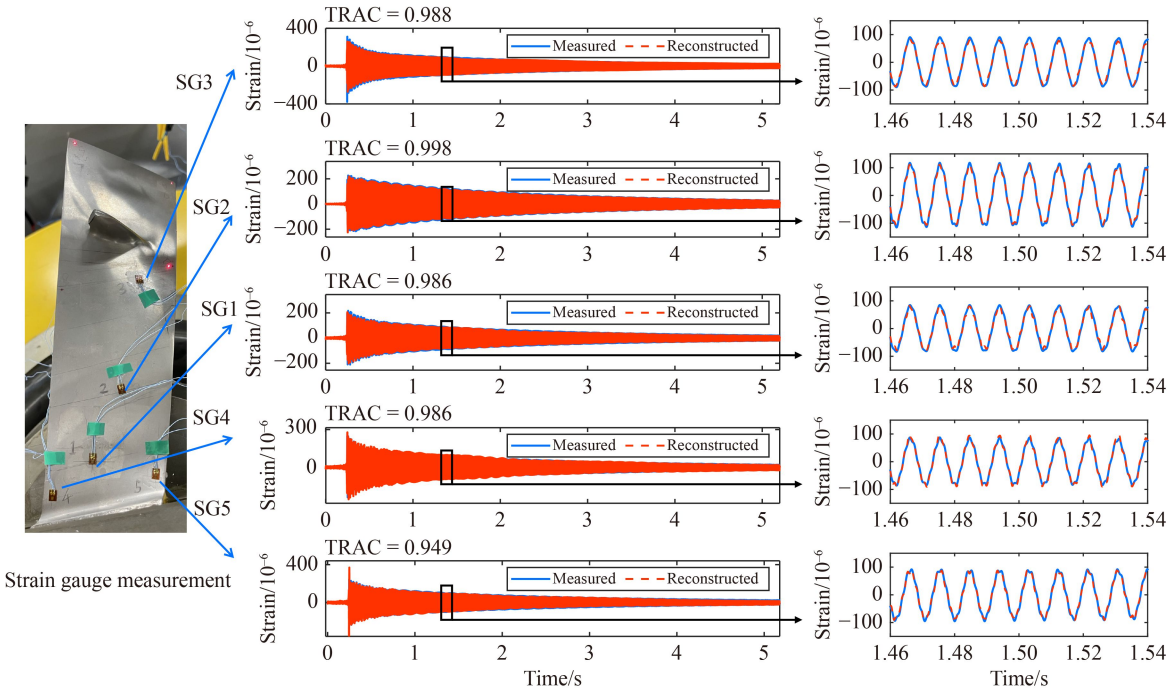

Fig. 12 Comparison of the measured strain by SGs and the reconstructed strain when the blade is excited by an impact force. SG: strain gauge, TRAC: time response assurance criterion.

whole blade in a non-contact manner but also enables a real-time strain reconstruction, where the traditional SG would fail. The reconstruction is realized by the displacement-to-strain transmissibility matrix derived in the modal coordinate based on the blade mode shapes. The proposed method is validated in numerical and experimental cases. The full-field strain is reconstructed using three displacement responses measured by laser triangulation sensors. The reconstructed responses of five points are compared with the SG measured results in the time domain. The high consistency between the reconstructed and measured results demonstrates that the proposed method enables an accurate strain prediction of the blade in single-mode and multi-mode vibration.

This study shows that the strain distribution and the position with max strain on the blade are unchanged with time when the blade vibrates under a single mode. However, when the blade vibrates under multiple modes, these distributions and positions would change on blades at different times. If all the changed strain distribution and the max strain need to be measured, then the SG may not complete the measurement. The method proposed in this paper can realize the real-time reconstruction of the strain distribution, thereby tracking the max strain on the blades. This would give comprehensive and accurate strain data for engineers to analyze the reliability and update the design of the blade. In addition, the proposed strain reconstruction technique has great potential in real-time measurements for blade vibration monitoring and residual life evaluation.

Nomenclature

Abbreviations

3D	Three-dimension
BTT	Blade tip timing
DIC	Digital image correlation
DST	Displacement-to-strain transmissibility
FE	Finite element
FRF	Frequency response function
HCF	High cycle fatigue
SEREP	System equivalent reduction expansion process
SG	Strain gauge
SLDV	Scanning laser Doppler vibrometer
TRAC	Time response assurance criterion

Variables

$\boldsymbol{C}$	Damping matrix
f	Natural frequency of the blade
f_1, f_2, f_3	First, second, and third natural frequencies, respectively
F, $\boldsymbol{F}$	Force and force vector, respectively
$\boldsymbol{F}(t)$, $\boldsymbol{F}(\omega)$	Force vector in the time and frequency domains, respectively
$\boldsymbol{H}(\omega)$	Displacement FRF matrix

i	Imaginary unit
j	Unmeasured/unknown dimension
k	Measured dimension
K_r, M_r, C_r	rth modal stiffness, mass, and damping of the blade, respectively
$\boldsymbol{K}$	Stiffness matrix
m	Number of the contributed modes
$\boldsymbol{M}$	Mass matrix
n	Node number of the blade finite element model
$\boldsymbol{P}$	Transformation between stress in the global and local coordinates
$q_1(t)$, $q_2(t)$, $q_3(t)$	First, second, and third mode contribution vectors, respectively
$\boldsymbol{q}$	Mode contribution matrix
$\boldsymbol{q}_r$	rth mode contribution vector
$\boldsymbol{q}(t)$, $\boldsymbol{q}(\omega)$	Mode contribution matrix in the time and frequency domains, respectively
$\boldsymbol{q}_r^{\mathrm{d}}(t)$, $\boldsymbol{q}_r^{\mathrm{d}}(\omega)$	Displacement contribution coefficient vectors of the rth mode in the time and frequency domains, respectively
$\boldsymbol{q}_r^{\varepsilon}(t)$, $\boldsymbol{q}_r^{\varepsilon}(\omega)$	Strain contribution coefficient vectors of the rth mode in the time and frequency domains, respectively
$\boldsymbol{S}$	Operator
$\boldsymbol{T}$	Displacement-to-strain transmissibility matrix
$\boldsymbol{x}$	Displacement response vector
$\boldsymbol{x}_{\mathrm{mear}}$	Measured displacement response
$\boldsymbol{x}_{\mathrm{unkn}}$	Unmeasured/unknown displacement response
$\boldsymbol{x}_{\mathrm{full}}$	Displacement response in the full dimension
$\boldsymbol{x}_x$, $\boldsymbol{x}_y$, $\boldsymbol{x}_z$	Displacement responses in the directions of X, Y, and Z, respectively
$\boldsymbol{x}(t)$, $\boldsymbol{x}(\omega)$	Displacement response in the time and frequency domains, respectively
ε_{e}	Equivalent strain
ε_x, ε_y, ε_z	Normal strains in the directions of X, Y, and Z of the global coordinate, respectively
$\varepsilon_{x'}$, $\varepsilon_{y'}$, $\varepsilon_{z'}$	Normal strains in the directions of X, Y, and Z of the local coordinate, respectively
$\boldsymbol{\varepsilon}$, $\boldsymbol{\varepsilon}'$	Strain matrixes in the global and local coordinates, respectively
$\boldsymbol{\varepsilon}_{\mathrm{full}}$	Strain response in the full dimension
$\boldsymbol{\varepsilon}_{\mathrm{mear}}$, $\boldsymbol{\varepsilon}_{\mathrm{recs}}$	Strain responses by measurement/simulation and reconstruction, respectively
$\boldsymbol{\varepsilon}(t)$, $\boldsymbol{\varepsilon}(\omega)$	Strain response in the time and frequency domains, respectively
α	Mass coefficient
β	Stiffness coefficient
σ_x, σ_y, σ_z	Normal stresses in the directions of X, Y, and Z of the global coordinate, respectively
$\sigma_{x'}$, $\sigma_{y'}$, $\sigma_{z'}$	Normal stresses in the directions of X, Y, and Z of the local coordinate, respectively
$\boldsymbol{\sigma}$, $\boldsymbol{\sigma}'$	Stress matrixes in the global and local coordinates, respectively
τ_{xy}, τ_{yz}, τ_{xz}	Shear stresses in the directions of XY, YZ, and XZ of the global coordinate, respectively
$\tau_{x'y'}$, $\tau_{y'z'}$, $\tau_{x'z'}$	Shear stresses in the directions of XY, YZ, and XZ of the local coordinate, respectively
γ_{xy}, γ_{yz}, γ_{xz}	Shear strains in the directions of XY, YZ, and XZ of the global coordinate, respectively
$\gamma_{x'y'}$, $\gamma_{y'z'}$, $\gamma_{x'z'}$	Shear strains in the directions of XY, YZ, and XZ of the local coordinate, respectively
ω	Exciting frequency
ω_r	Circular frequency of the rth mode
θ	Angle between one axis in the local coordinate and the other in the global coordinate
$\theta_{x'x}$, $\theta_{x'y}$, $\theta_{x'z}$, $\theta_{y'x}$, $\theta_{y'y}$, $\theta_{y'z}$, $\theta_{z'x}$, $\theta_{z'y}$, $\theta_{z'z}$	Angles between the local axises (x', y', and z') and the global axises (x, y, and z)
ξ_r	Damping ratio of the rth mode
$\boldsymbol{\Phi}$	Displacement mode shape
$\boldsymbol{\Phi}_1$, $\boldsymbol{\Phi}_2$, $\boldsymbol{\Phi}_3$	First, second, and third natural displacement mode shapes, respectively
$\boldsymbol{\Phi}_{\mathrm{full}}$	Displacement mode shapes in full dimension
$\boldsymbol{\Phi}_{\mathrm{mear}}$	Mode shape of the measured nodes
$\boldsymbol{\Phi}_{\mathrm{mear}}^{-1}$	Inverse matrix of $\boldsymbol{\Phi}_{\mathrm{mear}}$
$\boldsymbol{\Phi}_{\mathrm{mear}}^{\dagger}$	Moore–Penrose generalized inverse matrix of $\boldsymbol{\Phi}_{\mathrm{mear}}$
$\boldsymbol{\Phi}_r$	rth displacement mode shape
$\boldsymbol{\Phi}_{\mathrm{unkn}}$	Mode shape of the unmeasured nodes
$\boldsymbol{\Phi}_x$, $\boldsymbol{\Phi}_y$, $\boldsymbol{\Phi}_z$	Displacement mode shapes in the directions of X, Y, and Z, respectively
$\boldsymbol{\Psi}$	Strain mode shape
$\boldsymbol{\Psi}_{\mathrm{full}}$	Strain mode shapes in full dimension
$\boldsymbol{\Psi}_r$	rth strain mode shape
$\boldsymbol{\Psi}_x$, $\boldsymbol{\Psi}_y$, $\boldsymbol{\Psi}_z$, $\boldsymbol{\Psi}_{xy}$, $\boldsymbol{\Psi}_{yz}$, $\boldsymbol{\Psi}_{xz}$	Strain mode shapes in the directions of X, Y, Z, XY, YZ, and XZ, respectively
$\boldsymbol{\nabla}$	Linear differential operator

Acknowledgements This work was supported by the National Natural Science Foundation of China (Grant No. 52075414) and the National Science and Technology Major Project, China (Grant No. 2017-V-0009).

References

1. Chen X F, Wang S B, Qiao B J, Chen Q. Basic research on machinery fault diagnostics: past, present, and future trends.

Frontiers of Mechanical Engineering, 2018, 13(2): 264–291
2. Zhu Y P, Wang Y, Luo Z, Han Q K, Wang D Y. Similitude design for the vibration problems of plates and shells: a review. Frontiers of Mechanical Engineering, 2017, 12(2): 253–264
3. Ma H, Xie F T, Nai H Q, Wen B C. Vibration characteristics analysis of rotating shrouded blades with impacts. Journal of Sound and Vibration, 2016, 378: 92–108
4. Gao Y, Liu X Y, Xiang J W. FEM simulation-based generative adversarial networks to detect bearing faults. IEEE Transactions on Industrial Informatics, 2020, 16(7): 4961–4971
5. Yang F M, Yang Y M, Hu H F, Guan F J, Shen G J, Chen S Y, Bian Z F. Extraction of features due to breathing crack from vibration response of rotated blades considering tenon connection and shroud contact. Shock and Vibration, 2019, 2019: 8729620
6. Guo H T, Duan F J, Zhang J L. Blade resonance parameter identification based on tip-timing method without the once-per revolution sensor. Mechanical Systems and Signal Processing, 2016, 66–67: 625–639
7. Du Z H, Chen X F, Zhang H, Zi Y Y, Yan R Q. Multiple fault separation and detection by joint subspace learning for the health assessment of wind turbine gearboxes. Frontiers of Mechanical Engineering, 2017, 12(3): 333–347
8. Bouchain A, Picheral J, Lahalle E, Chardon G, Vercoutter A, Talon A. Blade vibration study by spectral analysis of tip-timing signals with OMP algorithm. Mechanical Systems and Signal Processing, 2019, 130: 108–121
9. Xu J H, Qiao B J, Liu M R, Yang Z B, Chen X F. Crack propagation monitoring of rotor blades using synchroextracting transform. Journal of Sound and Vibration, 2021, 509: 116253
10. Battiato G, Firrone C M, Berruti T M. Forced response of rotating bladed disks: blade tip-timing measurements. Mechanical Systems and Signal Processing, 2017, 85: 912–926
11. Poozesh P, Baqersad J, Niezrecki C, Avitabile P, Harvey E, Yarala R. Large-area photogrammetry based testing of wind turbine blades. Mechanical Systems and Signal Processing, 2017, 86(Part B): 98–115
12. Qiao B J, Ao C Y, Mao Z, Chen X F. Non-convex sparse regularization for impact force identification. Journal of Sound and Vibration, 2020, 477: 115311
13. Huh Y H, Kim J, Hong S G. Detection of local bonding failure damage by digital image correlation technique. Reliability Engineering & System Safety, 2019, 184: 21–26
14. Khadka A, Fick B, Afshar A, Tavakoli M, Baqersad J. Non-contact vibration monitoring of rotating wind turbines using a semi-autonomous UAV. Mechanical Systems and Signal Processing, 2020, 138: 106446
15. Retze U, Schüssler M. Dynamic Stress and Strain Measurement. Polytec Technical Papers, 2010
16. Sever I A, Maguire M. Correlation of full-field dynamic strain measurements with reverse engineered finite element model predictions. Experimental Techniques, 2021, 45(3): 377–387
17. Liu C H, Zang C P, Zhou B. Extension of continuous scanning laser Doppler vibrometry measurement for complex structures with curved surfaces. Chinese Journal of Aeronautics, 2020, 33(12): 3220–3227
18. Chen Y C, Escalera Mendoza A S, Griffith D T. Experimental and numerical study of high-order complex curvature mode shape and mode coupling on a three-bladed wind turbine assembly. Mechanical Systems and Signal Processing, 2021, 160: 107873
19. Vuye C, Vanlanduit S, Presezniak F, Steenackers G, Guillaume P. Optical measurement of the dynamic strain field of a fan blade using a 3D scanning vibrometer. Optics and Lasers in Engineering, 2011, 49(7): 988–997
20. Maguire M, Sever I. Full-field strain measurements on turbomachinery components using 3D SLDV technology. AIP Conference Proceedings, 2016, 1740(1): 080001
21. Luo W, Li J H, Ma X F, Wei W. A novel static deformation measurement and visualization method for wind turbine blades using home-made LiDAR and processing program. Optics and Lasers in Engineering, 2020, 134: 106206
22. Chen Y C, Joffre D, Avitabile P. Underwater dynamic response at limited points expanded to full-field strain response. Journal of Vibration and Acoustics, 2018, 140(5): 051016
23. Sarrafi A, Poozesh P, Niezrecki C, Mao Z. Mode extraction on wind turbine blades via phase-based video motion estimation. Proceeding SPIE 10171, Smart Materials and Nondestructive Evaluation for Energy Systems, 2017, 10171: 101710E
24. Baqersad J, Bharadwaj K. Strain expansion-reduction approach. Mechanical Systems and Signal Processing, 2018, 101: 156–167
25. Bharadwaj K, Sheidaei A, Afshar A, Baqersad J. Full-field strain prediction using mode shapes measured with digital image correlation. Measurement, 2019, 139: 326–333
26. Chen Z S, Sheng H, Xia Y M, Wang W M, He J. A comprehensive review on blade tip timing-based health monitoring: status and future. Mechanical Systems and Signal Processing, 2021, 149: 107330
27. Zhang X J, Wang Y R, Jiang X H, Gao S M. Blade vibration stress determination method based on blade tip timing simulator and finite element method. Journal of Engineering for Gas Turbines and Power, 2020, 142(3): 031001
28. Wang W M, Hu D F, Li Q H, Zhang X L. An improved non-contact dynamic stress measurement method for turbomachinery rotating blades based on fundamental mistuning model. Mechanical Systems and Signal Processing, 2020, 144: 106851
29. Mohamed M, Bonello P, Russhard P. A novel method for the determination of the change in blade tip timing probe sensing position due to steady movements. Mechanical Systems and Signal Processing, 2019, 126: 686–710
30. Wu S M, Zhao Z B, Yang Z B, Tian S H, Yang L H, Chen X F. Physical constraints fused equiangular tight frame method for blade tip timing sensor arrangement. Measurement, 2019, 145: 841–851
31. Bornassi S, Berruti T M, Firrone C M, Battiato G. Vibration parameters identification of turbomachinery rotor blades under transient condition using blade tip-timing measurements. Measurement, 2021, 183: 109861
32. Chakraborty A, Shishkin S, Birnkrant M J. Optimal control of build height utilizing optical profilometry in cold spray deposits. Proceeding SPIE 10168, Sensors and Smart Structures Technologies for Civil, Mechanical, and Aerospace Systems, 2017, 10168: 101683H
33. Kochkin D Y, Zaitsev D V, Kabov O A. Thermocapillary rupture

and contact line dynamics in the heated liquid layers. Interfacial Phenomena and Heat Transfer, 2020, 8(1): 1–9

34. Kranjc T, Slavič J, Boltežar M. A comparison of strain and classic experimental modal analysis. Journal of Vibration and Control, 2016, 22(2): 371–381
35. Rao S S, Atluri S N. The finite element method in engineering. Journal of Applied Mechanics, 1983, 50(4a): 914
36. Humar J. Dynamics of Structures. 3rd ed. Boca Baton: CRC Press, 2012
37. Zhou Y D, Tao J Y. Theoretical and numerical investigation of stress mode shapes in multi-axial random fatigue. Mechanical Systems and Signal Processing, 2019, 127: 499–512
38. Chen H, Song H W. Analysis of strain modals and the relationship between the strain modals and displacement modals. Noise and Vibration Control, 2016, 36(4): 7–13
39. Ao C Y, Qiao B J, Chen L, Xu J H, Liu M R, Chen X F. Blade dynamic strain non-intrusive measurement using $L_{1/2}$-norm regularization and transmissibility. Measurement, 2022, 190: 110677
40. Zhang X D. Matrix Analysis and Applications. Cambridge: Cambridge University Press, 2017
41. Kharyton V, Bladh R. Using tiptiming and strain gauge data for the estimation of consumed life in a compressor blisk subjected to stall-induced loading. In: Proceedings of the ASME Turbo Expo 2014: Turbine Technical Conference and Exposition. Volume 7B: Structures and Dynamics. Düsseldorf: ASME, 2014, V07BT33A028
42. Wu S M, Russhard P, Yan R Q, Tian S H, Wang S B, Zhao Z B, Chen X F. An Adaptive online blade health monitoring method: from raw data to parameters identification. IEEE Transactions on Instrumentation and Measurement, 2020, 69(5): 2581–2592
43. Duffy K P, Provenza A J, Bakhle M, Min J B, Abdul-Aziz A. Laser displacement measurements of fan blades in resonance and flutter during the boundary layer ingesting inlet and distortion-tolerant fan test. In: Proceedings of 2018 AIAA Aerospace Sciences Meeting. Kissimmee: AIAA, 2018
44. Aadnøy B, Looyeh R. Petroleum Rock Mechanics. Gulf Professional Publishing, 2011
45. Dowling N E. Mechanical Behavior of Materials: Engineering Methods for Deformation, Fracture, and Fatigue. 3rd ed. London: Pearson Prentice Hall Ltd., 2007
46. Wu Y, Liu G, Liu Z Q, Wang B. Formability and microstructure of Ti22Al24.5Nb0.5Mo rolled sheet within hot gas bulging tests at constant equivalent strain rate. Materials & Design, 2016, 108: 298–307
47. ANSYS I. Help System: Mechanical APDL Element Reference, 19.0. 2018
48. Kamaraj A V. Stress prediction in turbine blades under forced excitation. Thesis for the Master's Degree. San Diego: San Diego State University, 2016